This article was downloaded by: *[California Institute of Technology]*
On: *22 June 2010*
Access details: *Access Details: [subscription number 917270850]*
Publisher *Taylor & Francis*
Informa Ltd Registered in England and Wales Registered Number: 1072954 Registered office: Mortimer House, 37-41 Mortimer Street, London W1T 3JH, UK

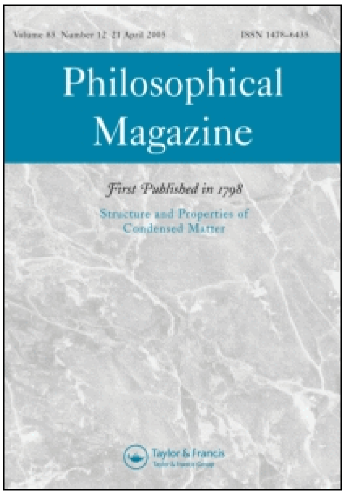

Philosophical Magazine
Publication details, including instructions for authors and subscription information:
http://www.informaworld.com/smpp/title~content=t713695589

A three-dimensional multiscale model of intergranular hydrogen-assisted cracking

J. J. Rimoli[a]; M. Ortiz[a]
[a] Division of Engineering and Applied Science, California Institute of Technology, Pasadena, CA 91125

Online publication date: 02 June 2010

To cite this Article Rimoli, J. J. and Ortiz, M.(2010) 'A three-dimensional multiscale model of intergranular hydrogen-assisted cracking', Philosophical Magazine, 90: 21, 2939 — 2963
To link to this Article: DOI: 10.1080/14786431003752134
URL: http://dx.doi.org/10.1080/14786431003752134

PLEASE SCROLL DOWN FOR ARTICLE

Full terms and conditions of use: http://www.informaworld.com/terms-and-conditions-of-access.pdf

This article may be used for research, teaching and private study purposes. Any substantial or systematic reproduction, re-distribution, re-selling, loan or sub-licensing, systematic supply or distribution in any form to anyone is expressly forbidden.

The publisher does not give any warranty express or implied or make any representation that the contents will be complete or accurate or up to date. The accuracy of any instructions, formulae and drug doses should be independently verified with primary sources. The publisher shall not be liable for any loss, actions, claims, proceedings, demand or costs or damages whatsoever or howsoever caused arising directly or indirectly in connection with or arising out of the use of this material.

Philosophical Magazine
Vol. 90, No. 21, 21 July 2010, 2939–2963

A three-dimensional multiscale model of intergranular hydrogen-assisted cracking

J.J. Rimoli* and M. Ortiz

Division of Engineering and Applied Science, California Institute of Technology, Pasadena, CA 91125

(*Received 28 December 2009; final version received 3 March 2010*)

We present a three-dimensional model of intergranular hydrogen-embrittlement (HE) that accounts for: (i) the degradation of grain-boundary strength that arises from hydrogen coverage; (ii) grain-boundary diffusion of hydrogen; and (iii) a continuum model of plastic deformation that explicitly resolves the three-dimensional polycrystalline structure of the material. The polycrystalline structure of the specimen along the crack propagation path is resolved explicitly by the computational mesh. The texture of the polycrystal is assumed to be random and the grains are elastically anisotropic and deform plastically by crystallographic slip. We use the impurity-dependent cohesive model in order to account for the embrittling of grain boundaries due to hydrogen coverage. We have carried out three-dimensional finite-element calculations of crack-growth initiation and propagation in AISI 4340 steel double-cantilever specimens in contact with an aggressive environment and compared the predicted initiation times and crack-growth curves with the experimental data. The calculated crack-growth curves exhibit a number of qualitative features that are in keeping with observation, including: an incubation time followed by a well-defined crack-growth initiation transition for sufficiently large loading; the existence of a threshold intensity factor K_{Iscc} below which there is no crack propagation; a subsequent steeply rising part of the curve known as *stage I*; a plateau, or *stage II*, characterized by a load-insensitive crack-growth rate; and a limiting stress-intensity factor K_{Ic}, or *toughness*, at which pure mechanical failure occurs. The calculated dependence of the crack-growth initiation time on applied stress-intensity factor exhibits power-law behavior and the corresponding characteristic exponents are in the ball-park of experimental observation. The stage-II calculated crack-growth rates are in good overall agreement with experimental measurements.

Keywords: hydrogen in metals; corrosion; polycrystalline metals; crack-growth; grain-boundary diffusion; multiscale modeling

1. Introduction

The work presented in this paper is concerned with the formulation and validation of a three-dimensional model of intergranular hydrogen-embrittlement (HE) that

---

*Corresponding author. Email: jjr@caltech.edu

ISSN 1478–6435 print/ISSN 1478–6443 online
© 2010 Taylor & Francis
DOI: 10.1080/14786431003752134
http://www.informaworld.com

accounts for: (i) the degradation of grain-boundary strength that arises from hydrogen coverage; (ii) grain-boundary diffusion of hydrogen; and (iii) a continuum model of plastic deformation that explicitly resolves the three-dimensional polycrystalline structure of the material. The present model builds on earlier work by Serebrinsky et al. [1] in several notable respects, including the three-dimensionality of the model, the addition of grain-boundary diffusion and the explicit resolution of the polycrystalline structure of the material, which was not accounted for in the earlier model. The increased fidelity of the present model enables a detailed assessment of the intricate interplay between growing cracks and material microstructure, including the effect of the local stress concentrations that arise from grain anisotropy and texture, the effect of differential plastic activity within the grains, and the discreteness of the available intergranular crack paths.

The accurate prediction of the lifetime of engineering components undergoing *environmentally assisted cracking* (EAC) poses a long-standing challenge in materials science. Owing to its complex nature, a number of widely differing mechanisms of EAC have been proposed [2–5]. In the present work we focus specifically on systems for which HE is recognized to be the dominant mechanisms. Such systems include high-strength steels in aqueous solutions and hydrogen-containing gaseous environments [6,7]. The effect of hydrogen on these systems is the result of three steps. In the first step, hydrogen is introduced into the metal via electrochemical charging, gaseous absorption, during fabrication, or from some other source. In the second step, atomic hydrogen is transported by diffusion to the crack tip [8,9]. In the third step, the hydrogen degrades the cohesive strength of the grain boundaries and results in premature failure at loads well below the toughness of the material *in vacuo*.

Hydrogen absorption may occur all along the growing length of the crack and can be described by means of appropriate boundary conditions [1,10]. These boundary conditions may in turn be related to transport in the crack environment and reactions at the crack surfaces [11,12]. Atomic hydrogen, being the smallest possible impurity, is generally considered to be transported easily by a combination of interstitial and intergranular diffusion [8,9]. However, the precise mechanism by which hydrogen embrittles metals has been the subject of considerable conjecture (e.g. [13] and references therein). Some of the proposed mechanisms are: (i) hydrogen-induced phase changes [14–16]; (ii) hydrogen-enhanced localized plasticity (HELP) [17,18]; and (iii) hydrogen-reduced cohesive energy [19–21].

The present work provides an indication that the combination of hydrogen transport and grain-boundary embrittlement can indeed account for the salient qualitative features, and results in fair quantitative agreement with, representative test data. In particular, we have carried out three-dimensional finite-element calculations of crack-growth initiation and propagation in AISI 4340 steel double-cantilever specimens in contact with an aggressive environment and compare the predicted initiation times and crack-growth curves with the experimental data of [22,23]. The polycrystalline structure of the specimen along the crack propagation path is accounted for explicitly by the finite-element mesh. The texture of the polycrystal is assumed to be random and the grains are elastically anisotropic and deform plastically by crystallographic slip. We use the impurity-dependent cohesive model put forth by Serebrinksy et al. [1], informed by the first-principles calculations of Jiang and Carter [24], in order to account for the embrittling of grain boundaries due to hydrogen coverage. The calculated crack-growth curves exhibit a number of qualitative features that are in keeping with observation, including: an incubation time followed by a well-defined crack-growth initiation transition for sufficiently large loading; intermittent crack growth, with quiescent periods alternating with discrete jumps, especially at high load levels; the existence of a threshold intensity factor K_{Iscc} below which there is no crack propagation; a subsequent steeply rising part of the curve known as *stage I*; a plateau, or *stage II*, characterized by a load-insensitive crack-growth rate; and a limiting stress-intensity factor K_{Ic}, or *toughness*, at which pure mechanical failure occurs. In addition, the calculated dependence of the crack-growth initiation time on applied stress-intensity factor exhibits power-law behavior and the corresponding characteristic exponents are in the ball-park of experimental observation. Finally, the stage-II calculated crack-growth rates are in good overall agreement with experimental measurements.

The paper is organized as follows. The details of the HE model are described in Section 2, including: the polycrystallization algorithm, Section 2.1; the crystal plasticity model, Section 2.2; the grain-boundary diffusion model, Section 2.3; and the coverage-dependent grain-boundary cohesive model, Section 2.4. Comparisons between calculated initiation times and crack-growth curves and the experimental data of [22,23] are presented in Section 3 by way of validation of the model. Finally, Section 4 collects concluding remarks and discussion.

2. Formulation of the model

The proposed model for intergranular stress corrosion cracking is based upon: (i) a continuum finite element model of the crystals including crystal plasticity; (ii) a grain boundary diffusion model informed with first-principles computations of diffusion coefficients; and (iii) an intergranular cohesive model described by concentration-dependent constitutive relations also derived from first-principles. A description of each aspect of the model is presented in the following subsections.

2.1. *Polycrystalline model*

We account for the polycrystalline structure of the material simply by resolving it with the finite element mesh. The polycrystallization algorithm that we follow for defining the geometry of the polycrystal is described in detail elsewhere and here we restrict ourselves to providing a brief summary in the interest of completeness. The definition of the polycrystal starts from a conventional tetrahedralization of the domain of analysis, Figure 1a, which greatly facilitates the handling of complex geometries. From this initial discretization we pass to its barycentric dual, cf. e.g. [25]. This operation defines a new discretization of the domain in which cells of dimension p are in correspondence with cells of dimension $3-p$ in the initial tetrahedralization, Figure 1b. Thus, in particular, the vertices of the initial tetrahedralization are in correspondence with the three-dimensional cells of the dual mesh, which we identify with as grains in the polycrystal; and the edges of the initial tetrahedralization are in correspondence with the two-dimensional facets that make up the grain boundaries. One important advantage of this barycentric dual

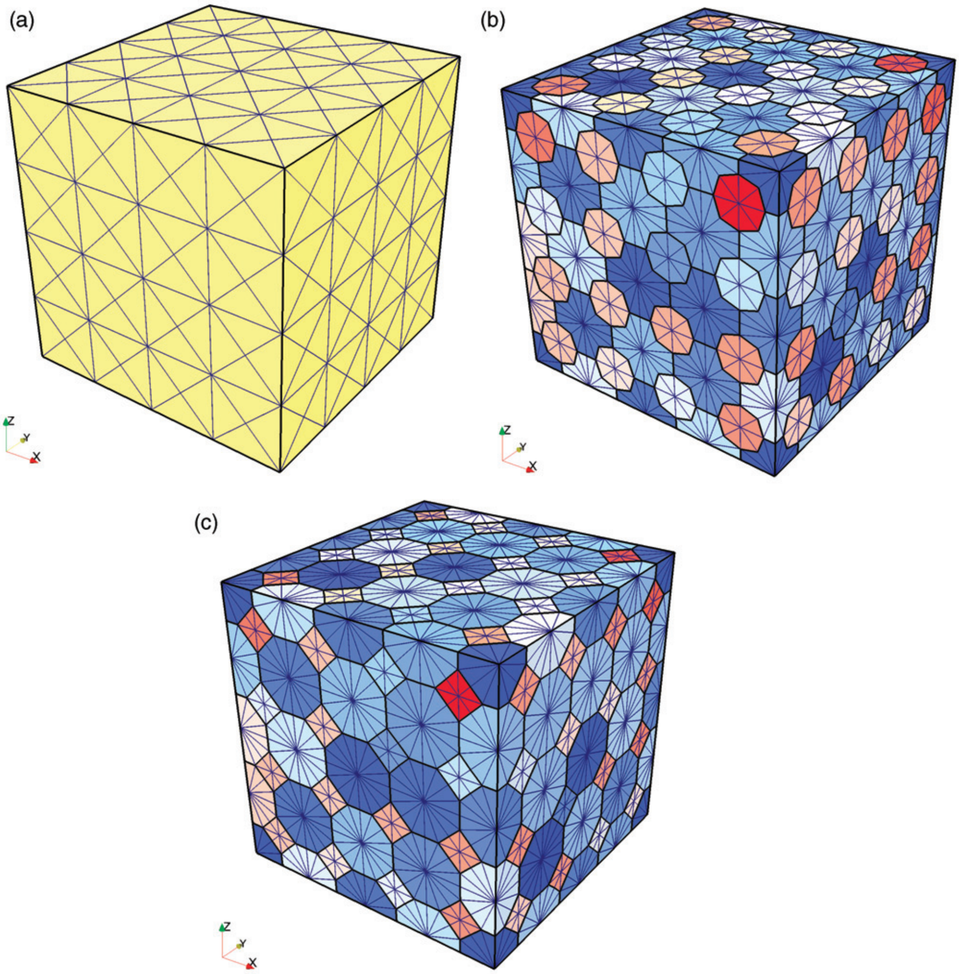

Figure 1. (Color online). Polycrystallization algorithm. (a) Initial tetrahedralization of the domain; (b) dual cell complex; and (c) dual cell complex with relaxed grain boundaries.

construction is that the cells in the dual, including grains and grain boundaries, terminate naturally at – and conform to – the boundary of the domain. In addition, the barycenter of each cell of the initial tetrahedralization is the site of a vertex, or node, in the barycentric dual. One shortcoming of this procedure is that it may generate some highly non-convex grains. In order to gain control on the shape of the grains and make it more physical we proceed to relax the grain boundaries. To that end we endow the grain boundaries with an energy proportional to their area and we allow the vertices in the barycentric dual to execute a gradient flow, i.e. to move in the direction of steepest descent of the energy. This type of surface kinetics is known as 'motion by curvature' and results in smoother and more convex grains (Figure 1c). Similar models have been effectively used in order to describe grain growth in polycrystals (cf. e.g. [26,27] and references therein). Finally, the computational mesh of the desired mesh size is generated by successive edge bisection.

Evidently, the geometry of the polycrystals defined by the algorithm just described is set by initial tetrahedralization of the domain. Specifically, the geometry of the polycrystal is defined by the placement of the vertices in the initial tetrahedralization and the precise manner in which they are triangulated. In all examples and calculations presented in this paper the initial tetrahedralization of the domain is chosen to be Delaunay. In the examples shown in Figure 1 and Figure 2a, the vertices in the initial tetrahedralization are placed in a body-centered cubic (BCC) arrangement. Evidently, the placement of the vertices in the initial tetrahedralization of the domain may be optimized so as to match grain and grain-boundary statistics (cf. e.g.[28,29] and references therein). However, these enhancements of the polycrystallization algorithm are beyond the scope of this paper and will not be pursued here.

2.2. *Crystal plasticity model*

HE results in brittle fracture at relatively low loads and, hence, the attendant deformations may be presumed small to a good approximation. We therefore describe the plastic deformation of the grains in the plastic zone surrounding the crack tip within the framework of linearized kinematics single-crystal plasticity. Thus, if u is the displacement field that described the deformation of the material, we assume that the strain tensor

$$\epsilon_{ij} = \frac{1}{2}(\partial_j u_i + \partial_i u_j) \tag{1}$$

admits an additive decomposition

$$\epsilon_{ij} = \epsilon^e_{ij} + \epsilon^p_{ij} \tag{2}$$

into a elastic part ϵ^e and a plastic part ϵ^p. The stress field then follows from Hooke's law as

$$\sigma_{ij} = c_{ijkl}\epsilon^e_{kl}, \tag{3}$$

whereas the plastic strain rate is assumed to obey conventional crystallographic slip kinematics of the form

$$\dot{\epsilon}^p_{ij} = \sum_{\alpha=1}^{N} \frac{\dot{\gamma}_\alpha}{2}(s_{\alpha i}m_{\alpha j} + s_{\alpha j}m_{\alpha i}) \tag{4}$$

where the sum runs over the slip systems of the crystal and the pair of unit orthogonal vectors $(s_{\alpha i}, m_{\alpha i})$ are the slip direction and slip-plane normal of slip system α, respectively. We further assume rate-independent behavior characterized by an isotropic power-law hardening of the form

$$\dot{\tau}_\alpha = \tau_0\left(\frac{\gamma}{\gamma_0}\right)^{1/n}\frac{\dot{\gamma}}{\gamma_0} \tag{5}$$

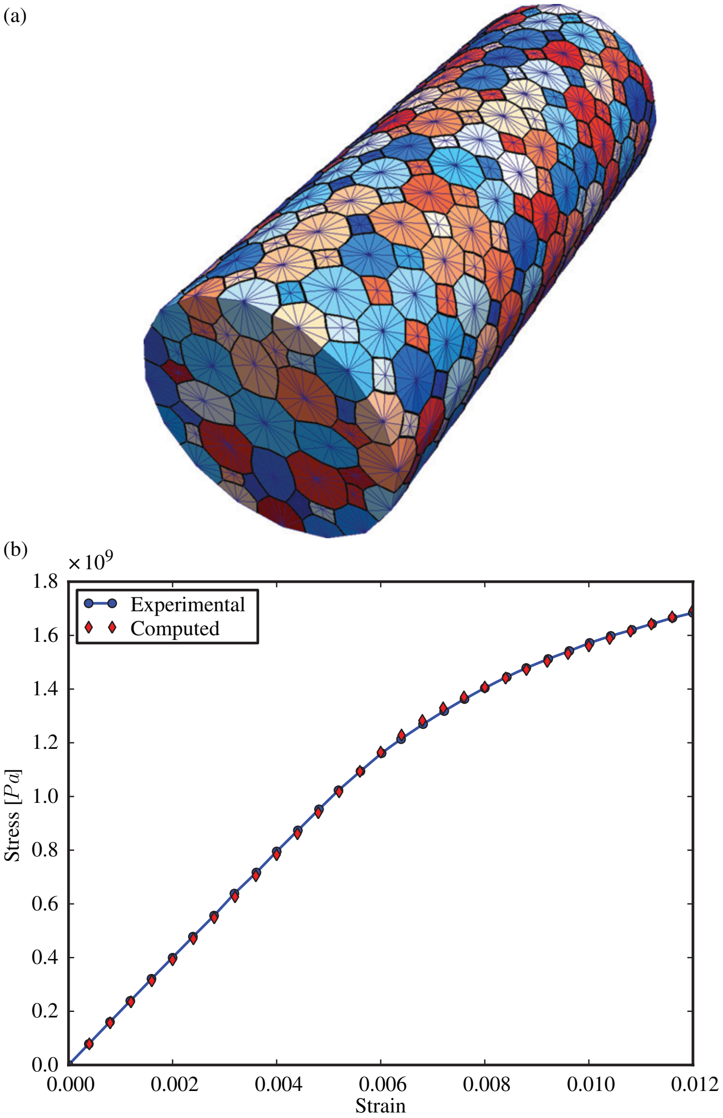

Figure 2. (Color online). Calibration of the single-crystal plasticity model for AISI 4340 steel. (a) Polycrystalline model used in calibration of plasticity model. (b) Comparison of experimental data (solids dots) [30] and model stress–strain curve (diamond symbols).

where τ_α is the critical resolved shear stress of slip system α, τ_0 is a reference critical resolved shear stress, γ_0 is a reference slip strain, n is the hardening exponent and

$$\dot{\gamma} = \sum_{\alpha=1}^{N} |\dot{\gamma}_\alpha|. \tag{6}$$

The governing equations, including the loading-unloading conditions, are closed by means of the Kuhn–Tucker loading conditions [31]

$$\dot{\gamma}_\alpha \geq 0, \tag{7a}$$

$$\tau_\alpha \sigma_{ij} - s_{\alpha i} m_{\alpha j} \leq 0, \tag{7b}$$

$$(\sigma_{ij} s_{\alpha i} m_{\alpha j} - \tau_\alpha)\dot{\gamma}_\alpha = 0. \tag{7c}$$

In calculations, the preceding governing equations are integrated in time by means of a variational update [32], which ensures the symmetry of the tangent stiffness and ensures convergent approximations in the limit of vanishingly small time steps.

The steels of primary interest here crystalize in the body-centered crystal class and the corresponding slip systems are the family of systems of the type {211}[111] and {110}[111]. In addition, the elastic moduli of the crystals exhibit cubic symmetry as well. Figure 2b shows the calibration of the crystal plasticity model for AISI 4340 steel [30]. The polycrystalline stress–strain curve used for calibration is obtained from the representative polycrystalline volume shown in Figure 2a endowed with random texture. The material constants identified through this calibration are tabulated in Table 2.

2.3. *Grain boundary diffusion model*

We are specifically concerned with the diffusion of hydrogen in metals containing cracks in contact with an aggressive environment. We assume that the mechanisms by which hydrogen is transported to the crack tip are absorption at the boundary, bulk diffusion and grain boundary diffusion. Consideration of these mechanisms leads to the formulation of a stress-assisted diffusion problem. We model hydrogen diffusion by recourse to Fisher's model [33–35]. We specifically focus on type C kinetics [36] such as are expected to dominate at room temperature and large grain sizes. In this regime, the bulk diffusion is nearly locked and diffusion takes place almost exclusively at the grain boundaries, without any essential leakage to the neighboring grains. Under these conditions, for planar grain boundaries Fisher's model reduces to the two-dimensional diffusion equation

$$\frac{\partial C}{\partial t} = \nabla \cdot (D_{gb} \nabla C), \tag{8}$$

where $C(x_1, x_2, t)$ is the hydrogen concentration on the plane of the grain boundary, ∇ and $\nabla\cdot$ are the two-dimensional gradient and divergence operators and D_{gb} is the grain-boundary diffusivity tensor.

We have identified the grain diffusivity of hydrogen in iron grain boundaries from the results of first-principles calculations collected in Table 1 [37]. The methodology used in these calculations is described in detail in [38–40]. For simplicity, in calculations we assume that the grain-boundary diffusivity is isotropic and obeys an Arrhenius law. These approximations result in a temperature-dependent scalar grain-boundary diffusivity of the form

$$D_{gb}(T) = D_0 \exp\left(-\frac{T_0}{T}\right), \tag{9}$$

where the constants can be obtained by averaging the diffusion data in Table 1, with the result $D_0 = 2.44 \cdot 10^{-7}\,\mathrm{m}^2/\mathrm{s}$, $T_0 = 1334.42\,\mathrm{K}$. It should be noted that grain-boundary diffusivity is generally lower than free-surface diffusivity (e.g. [41]). Consequently, the diffusivity of a grain-boundary may be expected to decrease towards the corresponding free-surface diffusivity as the grain-boundary opens to form a crack. However, the precise dependence of grain-boundary diffusivity on opening displacement is poorly understood at present and in calculations we simply neglect this effect by keeping grain-boundary diffusivities constant.

The formulation of appropriate boundary conditions for the diffusion of hydrogen in a metal in contact with an aggressive environment also poses significant challenges. Following [1], three main regions of the boundary may be

Table 1. Hydrogen diffusivity in iron grain-boundaries (Å/ps)[37].

Type of GB	D_{gb} at 500 K	D_{gb} at 1500 K
Σ3[110][111]	2.82	16.18
Σ5[001][210]	1.13	6.73
Σ5[001][310]	1.61	9.57
Σ7[111][321]	2.01	12.40
Σ13[001][320]	1.53	9.08
Σ13[001][510]	1.34	7.98
Σ17[001][530]	1.39	8.25
Average	1.69	10.03

Table 2. Material properties used in calculations.

Property	Value
Crystal structure	BCC
Slip planes	$\{\underline{1}10\}$
Slip directions	$\langle\bar{1}11\rangle$
# of slip systems	24
Grain size	≈100μm
C_{11}	208.9 GPa
C_{12}	126.4 GPa
C_{14}	97.7 GPa
τ_0	570.0 MPa
γ_0	0.01
n	0.80
K_{Ic}	58.4 MPa
$\bar{\sigma}_c$	5.6 GPa
$\bar{\delta}_c$	1.03μm
D_{gb}	$2.53 \cdot 10^{-9}$ m^2/sec

identified: (i) the exterior surface of the body; (ii) the crack flanks, and (iii) the cohesive zones at the tip of the cracks. Over the crack flanks the metal may be assumed to be in equilibrium with the environment, which requires the chemical potential of the metal and an external chemical potential representative of the environment to be exactly balanced. This condition in turn requires that the hydrogen concentration on the crack flanks equal a pressure and temperature dependent equilibrium concentration [1]. In aqueous environments, the external chemical potential may vary along the crack flanks. For instance, hydrolysis of highly concentrated metal ions generates a localized acidified medium [12,42], giving an enhanced source of hydrogen. However, Sharland and Tasker [43] have shown that such variations are negligible up to very small distances from the crack mouth.

Partially open grain boundaries may be expected to exhibit hydrogen absorption characteristics intermediate between bulk, i.e. no absorption, and free surface. Nguyen accounted for this effect by means of mixed Dirichlet–Neumann boundary conditions [44], consisting of prescribing a linear combination of concentration and normal flux. The coefficients of this linear combination are made to depend on the crack opening so as to achieve a continuous transition between a zero flux boundary condition at zero crack opening and a free-surface boundary condition on fully decohered grain-boundaries. However, the conditions prevailing in the environment immediately adjacent to crack tips are complex and do not appear to be entirely understood at present. For instance, Lu et al. [45] found evidence suggesting that for 4340 steel strained in gaseous H_2S, at 0.133 kPa and below room temperature, the crack propagation rate was controlled by transport in the gas phase, an indication that transport of gas into partially open grain boundaries is restricted and a rate-limiting effect. More complex yet are the conditions present in aqueous environments due to localized acidification and other complex effects.

In view of the complexity of the interactions between a crack and an aggressive environment – and the imperfect understanding of those interactions – in calculations we adopt the simplest of boundary and initial conditions. Thus, on the flanks of the initial crack we assume that the environment is sufficiently aggressive that the coverage remains at its saturation level. We also assume that grain-boundary and surface coverage is continuous at the points of intersection between grain boundaries and free surfaces. These assumptions give the condition for the coverage $\theta = 1$ on the initial flanks of the crack. We additionally assume no penetration of the aggressive environment into partially or fully decohered grain-boundaries and, hence, the coverage of grain boundaries remains controlled by grain-boundary diffusion at all times.

2.4. *Cohesive laws accounting for impurity segregation*

As in the preceding work of Serebrinksy et al. [1], the centerpiece of the present approach is a cohesive model of fracture which accounts for the effect of impurity segregation. In calculations, we use the impurity-dependent cohesive model put forth by Serebrinksy et al. [1], which we proceed to summarize briefly in the interest of completeness. Grain-boundary fracture may be described by means of a cohesive law that governs the separation of the grain boundary. Hydrogen embrittlement may then be modeled through the weakening of the cohesive law commensurate with the hydrogen coverage of the grain boundary. In the present work, the transport of hydrogen to the grain boundary is assumed to occur as a result of grain boundary diffusion, as described in the foregoing. However, as noted by Serebrinksy et al. [1], the effect of impurities such as hydrogen on cohesive laws in metals cannot be elucidated classically but requires a full quantum-mechanical treatment.

Suppose, for definiteness, that the atomic level interplanar normal traction-separation relation is well approximated by the UBER form [46]

$$\sigma = A\,\delta\,\mathrm{e}^{-\delta/\delta_c}\ , \tag{10}$$

where δ is the normal opening displacement, σ is the normal cohesive traction, and δ_c is the critical separation at which σ attains its maximum value

$$\sigma_c = e^{-1} A\,\delta_c\ . \tag{11}$$

In addition,

$$2\,\gamma = e\,\sigma_c\,\delta_c \tag{12}$$

is the surface energy of the grain boundary. The calculations of van der Ven and Ceder [47] suggest that δ_c is insensitive to coverage and, therefore, can be taken to be constant to a first approximation. By contrast, the cohesive strength σ_c depends sensitively on coverage. A fit to the data of Jiang and Carter [24] for the H/bcc Fe(110) system, Figure 3a, then gives

$$\gamma(\theta) = (1 - 1.0467\,\theta + 0.1687\,\theta^2)\,\gamma_0 \tag{13}$$

where $\theta = C/C_s$ is the grain-boundary coverage, C is the surface hydrogen concentration, C_s is its saturation value, $\gamma(\theta)$ is the grain-boundary surface energy at coverage θ and γ_0 is the grain-boundary surface energy at zero coverage. Transferring the dependence of $\gamma(\theta)$ to σ_c through relation (12) gives

$$\sigma_c(\theta) = \frac{2\gamma(\theta)}{e\delta_c}, \tag{14}$$

which completely determines the atomic-level cohesive law for normal separation.

Two main difficulties must be overcome in order to use the impurity-dependent cohesive law just derived in macroscopic calculations. Firstly, the normal cohesive law must be extended to general three-dimensional opening displacements. A simple device for effecting that extension, which we adopt in our calculations, is to introduce an effective normal opening displacement [48]. Secondly, the atomic-level cohesive law entails inordinately high cohesive strengths of the order of the theoretical strength of the material, and exceedingly small critical opening displacements of the order of the interplanar separation. A direct use of the atomic-level cohesive law in finite element calculations would then require mesh sizes of the order of the atomic lattice in order to obtain converged solutions [49]. This essential difficulty may be overcome by renormalizing the cohesive law from the

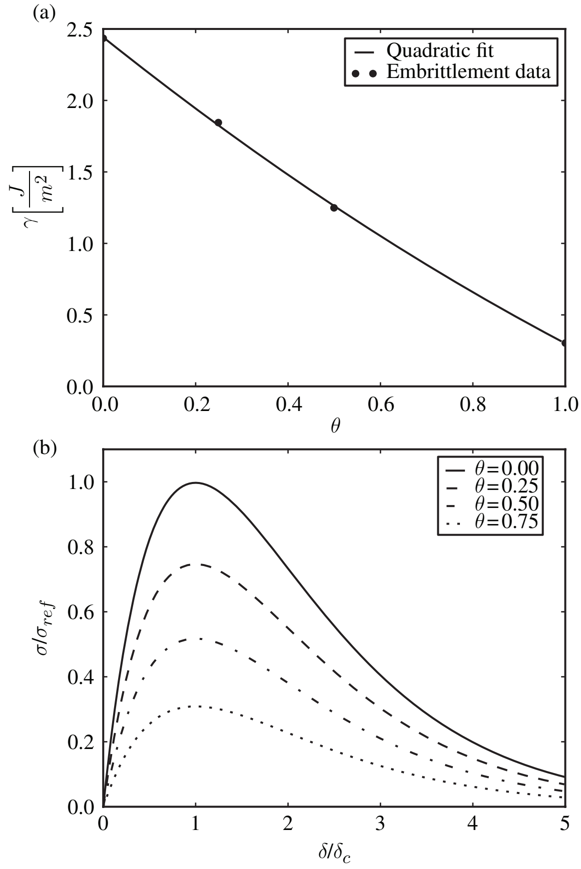

Figure 3. (a) Effect of hydrogen on cohesive energy of bcc Fe(1 1 0). First principles computations [24] (solid circles) and quadratic fit (line). (b) Traction-reparation law for different values of impurity coverage θ for H in Fe.

atomic scale to the scale of the finite-element resolution [50]. The resulting renormalized cohesive strength and critical opening displacement are

$$\bar{\sigma}_c = \sqrt{\frac{d}{h}}\sigma_c, \tag{15a}$$

$$\bar{\delta}_c = \sqrt{\frac{h}{d}}\delta_c, \tag{15b}$$

respectively, where d is a grain-boundary interplanar separation and h is the macroscopic mesh size. In addition, the renormalized cohesive-zone size scales as h/d, with the result that it is resolved by the mesh, as required for convergence. In this manner, the renormalization procedure thus enables the use of the atomic-scale cohesive law in finite-element calculations.

There are different criteria for the selection of the value of $\bar{\sigma}_c$, and its value will have an impact in the competition between the plastic and decohesion processes in the polycrystal. A parametric study could be performed to asses the effects of this competition, but it is clearly beyond the scope of our work. In calculations, for the given fracture toughness K_{Ic} the value of $\bar{\sigma}_c$ is chosen so that the cohesive-zone length is resolved by the mesh. That is, $\bar{\sigma}_c = \sqrt{K_{Ic}^2(1-\nu^2)/l_c}$, where K_{Ic} is the fracture toughness of the material, ν its Poisson's ratio and l_c the cohesive zone length. The adopted value for the cohesive zone length is on the order of the grain size, i.e. $l_c = 100\mu\text{m}$. The value of $\bar{\delta}_c$ is then uniquely determined by K_{Ic} and $\bar{\sigma}_c$ as $\bar{\delta}_c = G_c/(e\sigma_c)$ with $G_c = K_{Ic}^2(1-\nu^2)/E$, being E the Young's modulus of the material. The corresponding values for $\bar{\sigma}_c$ and $\bar{\delta}_c$ are displayed on Table 2.

3. Model validation examples

We proceed to validate the model of hydrogen embrittlement described in the foregoing by means of comparisons to selected initiation-time data [22] and crack-growth-rate data [23] on compact specimens. We specifically consider AISI 4340 steel undergoing stress corrosion cracking in an aqueous solution, a configuration that is generally agreed to result in hydrogen assisted cracking [51]. Compact test specimens are often machined from plates which are in turn cut from hot rolled round bars. The specimens are then electropolished and coated to avoid hydrogen contamination. In initiation-time tests, the specimen is loaded and the incubation time for the onset of crack propagation is measured, e.g. by an electrical potential method. In this method of measurement, a constant current is applied to the specimen and the voltage difference through the notch mouth is measured. The tests are interrupted and the initiation time is recorded when a potential increase is observed. In crack-growth-rate tests, the specimen is loaded and the crack length is measured by means of a traveling microscope. In addition, a clip gage is sometimes mounted in order to measure the crack growth behavior with increased sensitivity. The crack-growth rate is then computed by numerical differentiation of the crack length history.

3.1. *Computational model and solution procedure*

The solution procedure employed in calculations consists of two stages: initialization and time integration. During the initialization stage, the geometry is generated and the boundary conditions for the diffusion problem are imposed. Afterwards, the cohesive law is updated to reflect the given impurity concentration distribution across the specimen. Finally, the mechanical pre-load is imposed incrementally until the desired stress intensity factor is reached.

The geometry, dimensions and layout of the computational model are shown in Figure 4. The calculations concern a double-cantilever specimen of dimensions $2.5 \times 0.625 \times 0.3125\,\text{mm}$ containing a sharp precrack of size 1.25 mm. A number of simplifying approximations are made in order speed up the calculations. Firstly, the full polycrystalline geometry is restricted to a gage section of dimensions $1.0 \times 0.625\,\text{mm}$ bounding the initial crack tip and the crack propagation path.

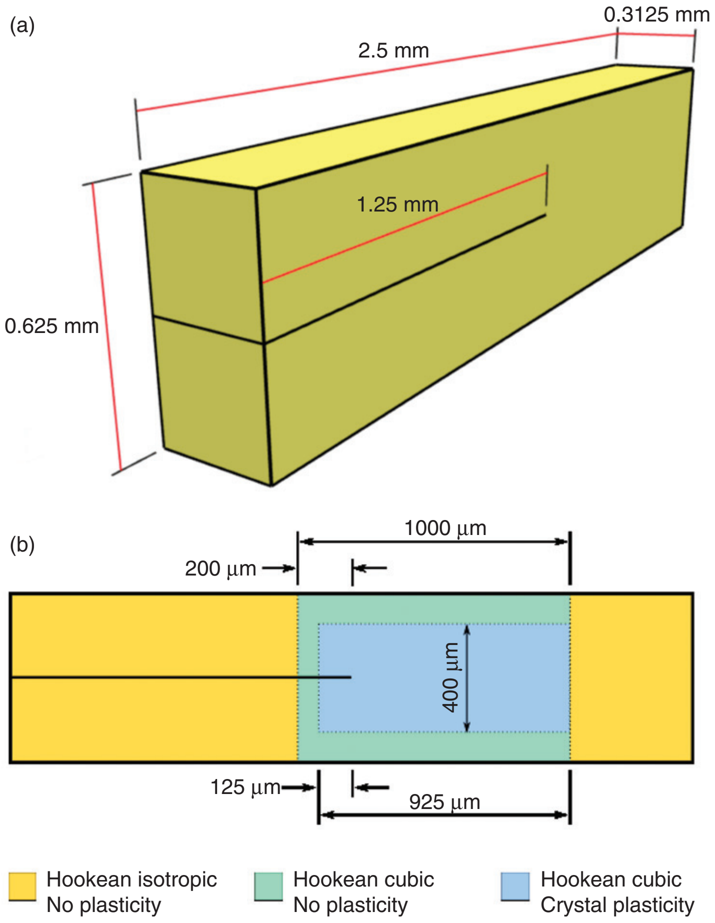
(a)
0.3125 mm
2.5 mm
1.25 mm
0.625 mm
(b)
1000 μm
200 μm
400 μm
125 μm
925 μm
Hookean isotropic
No plasticity
Hookean cubic
No plasticity
Hookean cubic
Crystal plasticity

Figure 4. (Color online). Double-cantilever AISI 4340 steel specimen. (a) Geometry of the computational model. (b) Subdomains and levels of approximation employed in calculations.

Crystal plasticity is further restricted to a small gage section of dimensions 0.925×0.4 mm of sufficient size to contain the plastic zone. The remainder of the computational domain is idealized as isotropic linear elastic. The geometry and the mesh of the polycrystal gage region is generated using the polycrystallization algorithm described in Section 2.1, and the texture of the polycrystal is assumed to be random. The remainder of the mesh is rapidly coarsened away from the gage region. In order to avoid volumetric locking due to nearly-isochoric plasticity near the crack tip, the polycrystalline region is discretized by means of constant-pressure tetragonal elements enriched with quadratic face bubbles. These elements can be shown to exactly satisfy the inf-sup convergence condition for incompressible linear elasticity, e.g. by considering a two-element macroelement [52]. The resulting computational model contains a total 600 grains, in the order of 80,000 tetrahedral elements and 300,000 degrees of freedom.

The diffusion problem is discretized by means of linear triangular elements placed on the grain boundaries and integrated in time by the forward-Euler algorithm. At the end of every diffusion time step, the interpolated impurity concentration is sampled at the quadrature points of the cohesive elements and input into the impurity-dependent cohesive law, which effectively couples the diffusion and fracture problems. The grain-boundary diffusion model has 12,000 degrees of freedom only and its execution times are negligible compared to the execution times of the mechanical model.

The time evolution of the system is followed by means of a staggered procedure [53]. Thus, after executing a diffusion step, the hydrogen concentration is interpolated from the nodal values of the grain-boundary diffusion elements to the quadrature points of the cohesive elements. At those points, the cohesive law is then updated accordingly. Subsequently, a mechanical step solves the quasistatic equilibrium problem by means of a combination of dynamic relaxation [54,55] and a Newton–Raphson iteration, thus completing one step of the staggered procedure. The robustness of dynamic relaxation proves essential during crack propagation, which often takes places through discrete jumps. At such transitions, the system overcomes energy barriers and generally negotiates a complex energy landscape and the Newton–Raphson iteration almost invariably fails to converge. In calculations, dynamic relaxation is applied first in order to place the system in the domain of convergence of the Newton–Raphson iteration, which is then used to equilibrate the system to a high degree of precision.

The mechanical boundary conditions consist of prescribed opening displacements on the top and bottom surfaces of the double-cantilever beam specimen, applied instantaneously at the beginning of the calculations, and traction-free boundary conditions elsewhere. The model was calibrated for an isotropic linear-elastic specimen in order to determine the factor of proportionality between the nominal applied stress-intensity factor K_I and the prescribed opening displacement. This calibration enables the reduction of the results of calculations in terms of K_I. The boundary conditions for the diffusion problem consist of a prescribed full coverage over a 0.2 mm region of the crack flanks adjacent to the initial crack front, representing the action of an aggressive environment, and a zero-flux condition elsewhere. The material properties employed in the simulations are summarized Table 2. In this table, C_{11}, C_{12} and C_{14} and the elastic moduli of the cubic grains, τ_0 is the critical resolved shear stress, γ_0 is a reference slip strain, n is the hardening exponent, K_{Ic} is the toughness and D_{gb} is the average grain-boundary diffusion.

3.2. *Results of simulations*

Figures 5, 6 and 7 showcase selected outcomes of the calculations at a high applied stress-intensity factor $K_I = 41.2\,\mathrm{MPa}\sqrt{\mathrm{m}}$ close to the toughness of the material, $K_{Ic} = 58.4\,\mathrm{MPa}\sqrt{\mathrm{m}}$. Specifically, Figure 5 shows the evolution of hydrogen coverage on grain boundaries. As expected, hydrogen is transported from the environment by diffusion and causes the grain boundaries near the crack front to weaken. Eventually, the grain boundaries become brittle enough that the crack starts growing and outruns the hydrogen affected zone near the initial crack front, Figure 6.

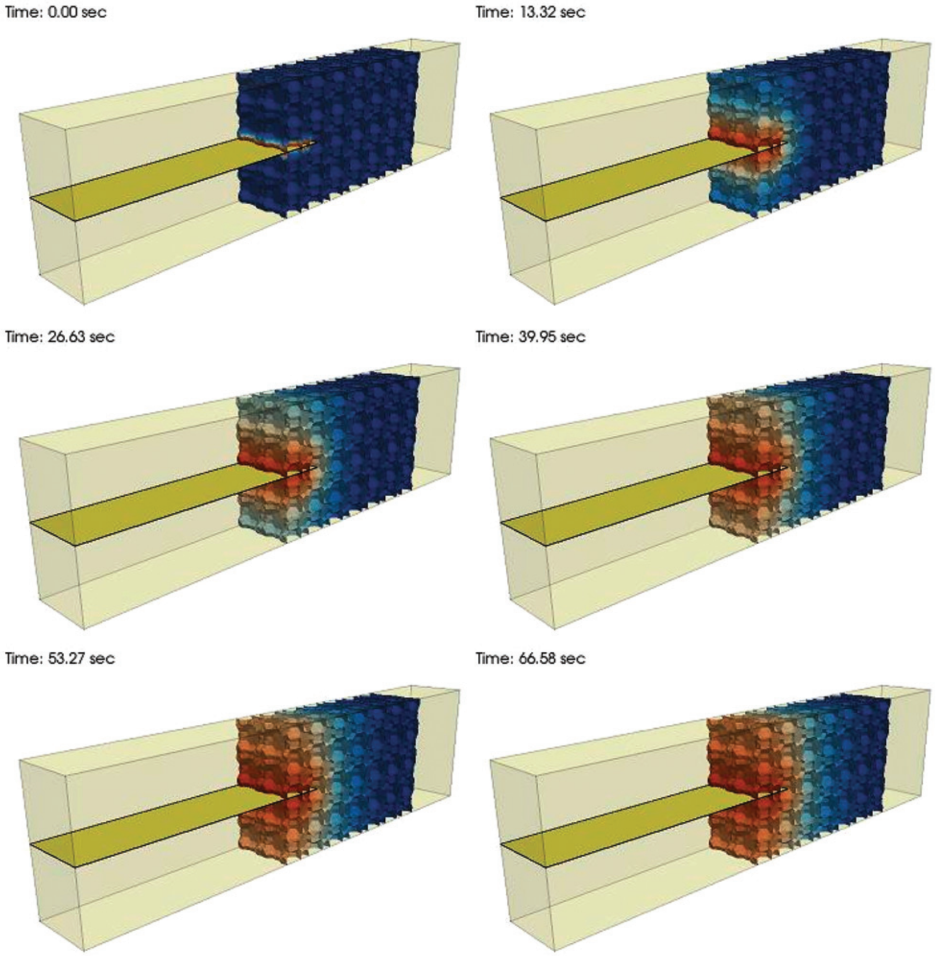

Figure 5. (Color online). Double-cantilever AISI 4340 steel specimen subjected to a constant applied stress-intensity factor $K_I = 41.2\,\mathrm{MPa}\sqrt{\mathrm{m}}$ in an aggressive environment. Temporal evolution of hydrogen coverage of grain boundaries.

The evolution of the crack surface and the crack front, which is assumed to be intergranular in the present model, is strongly three-dimensional and exhibits phases of crack kinking and trapping, as the crack propagates over and around the grains. The complex interactions between the crack front and individual grains causes the crack growth to be jerky and unsteady. At lower loading rates, the crack front does not outrun the hydrogen affected zone, or does so to a lesser extent, and crack growth tends to be more steady, cf. Section 3.3. Evidently, these inherently three-dimensional crack-growth mechanisms cannot be accounted for by a two-dimensional model such as considered in [1]. Indeed, the careful consideration of three-dimensional crack-growth effects on the scale of the polycrystalline structure

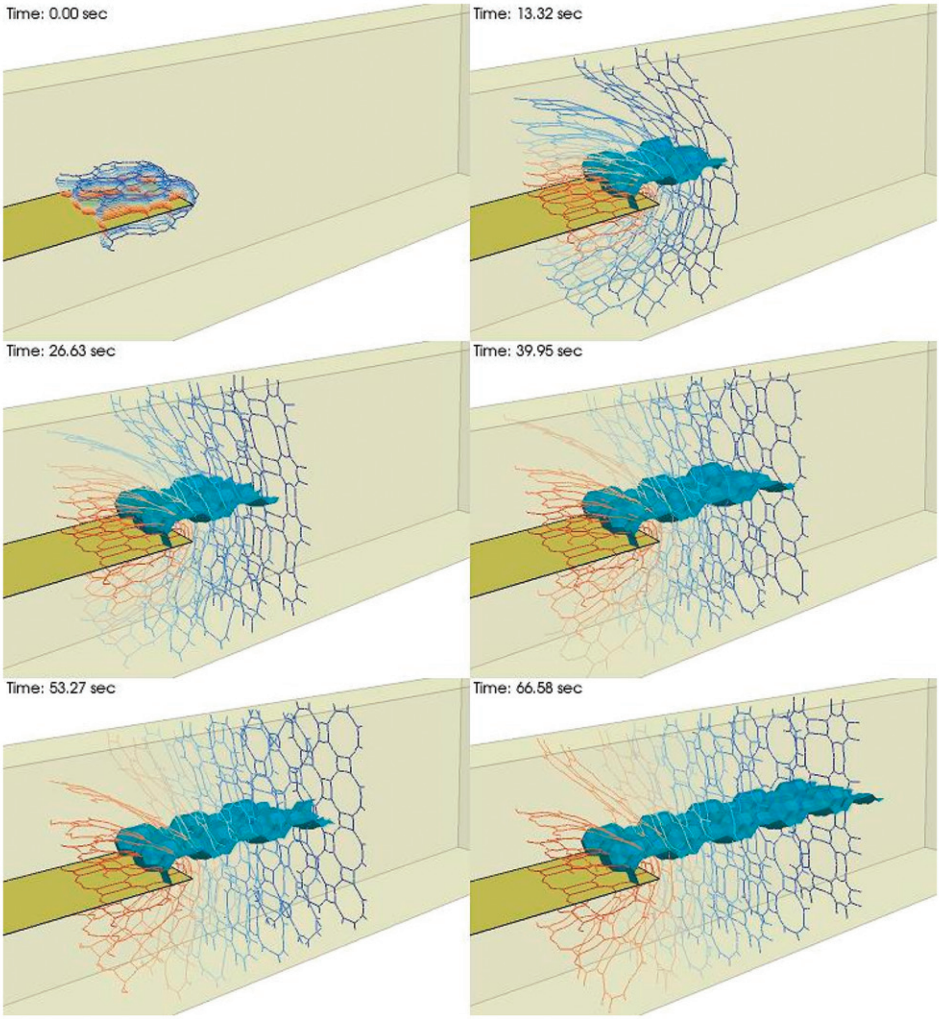

Figure 6. Double-cantilever AISI 4340 steel specimen subjected to a constant applied stress-intensity factor $K_I = 41.2\,\mathrm{MPa}\sqrt{\mathrm{m}}$ in an aggressive environment. Temporal evolution of the crack surface. Color-coded contour levels represent the hydrogen coverage. The fracture surface is shown in light blue.

is one of the ways in which the present work extends that earlier two-dimensional model. A second modeling enhancement that is afforded by a three-dimensional model is the explicit consideration of texture, grain-to-grain elastic anisotropy and single-crystal plasticity. Thus, Figure 7 presents a side view of plastic activity, as measured by contours of effective plastic strain γ, Equation (6), cf. Section 2.2. Interestingly, even at a relatively high applied stress-intensity factor approaching the toughness of the material, the initial plastic zone is confined within one grain. Subsequent crack growth induces further plastic activity, which is also confined to

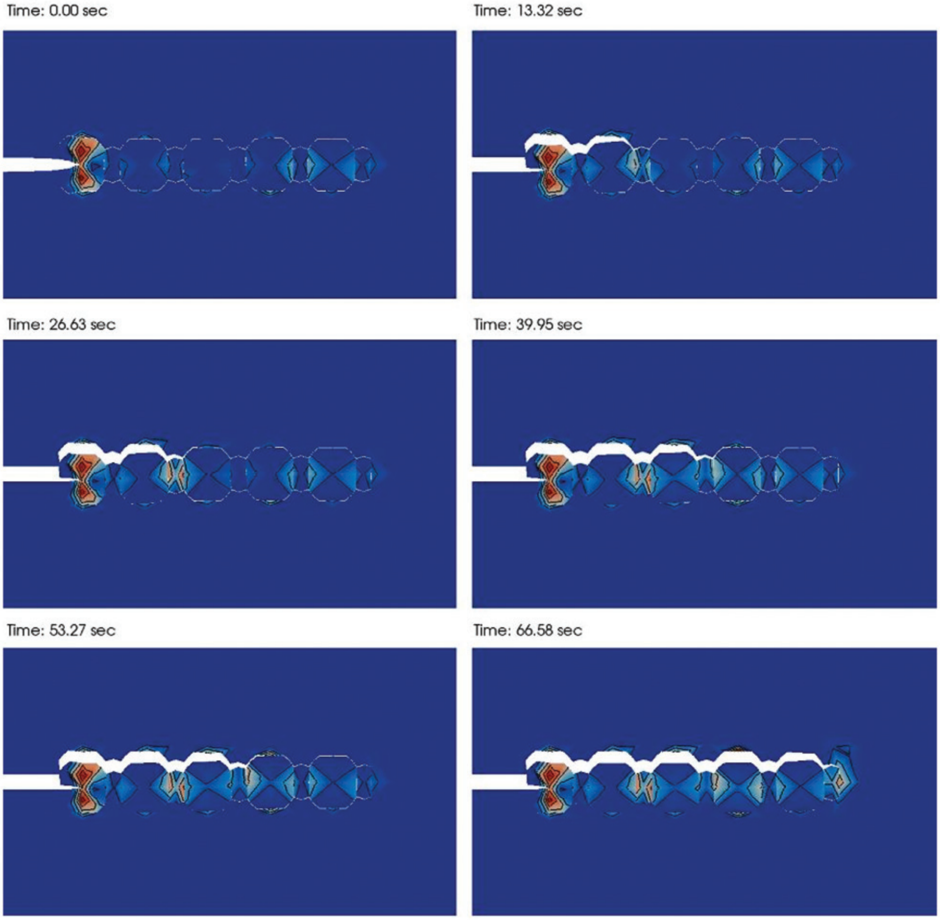

Figure 7. (Color online). Double-cantilever AISI 4340 steel specimen subjected to a constant applied stress-intensity factor $K_I = 41.2\,\text{MPa}\sqrt{\text{m}}$ in an aggressive environment. Lateral view of the temporal evolution of crack surface and attendant plastic activity in the grains. Color coded contours represent levels of effective plastic strain.

single grains neighboring the crack front. Despite the small size of the plastic zone, crystal plasticity does effectively relax the level of stress in the vicinity of the crack tip and partially shields the decohering grain boundaries, thus retarding crack growth.

3.3. *Crack length vs. time*

The computed crack length is plotted in Figure 8 as a function of time for applied stress-intensity factors K_I ranging from 13.7 to $41.2\,\text{MPa}\sqrt{\text{m}}$. Specifically, the crack length is computed as the ratio of the area of fully decohered cohesive elements, i.e. cohesive elements such that $\delta > \delta_c$, to the thickness of the specimen.

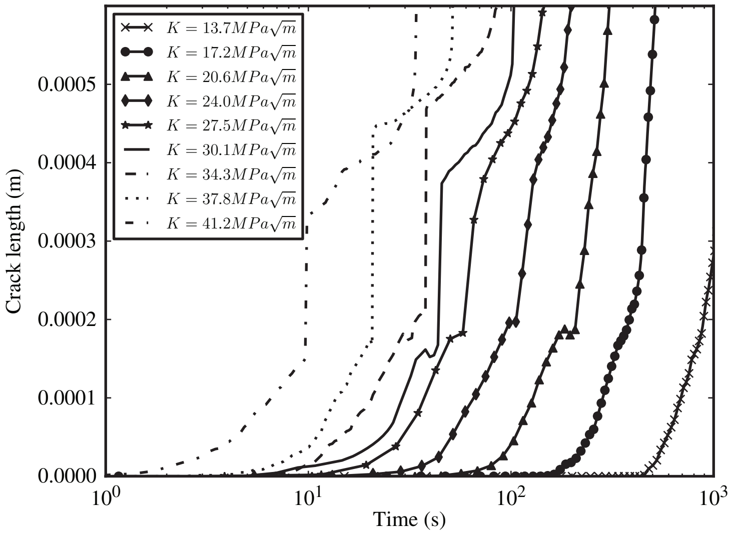

Figure 8. Double-cantilever AISI 4340 steel specimen subjected to a constant applied stress-intensity factor in an aggressive environment. Crack length evolution for applied stress-intensity factors ranging from 13.7 to 41.2 MPa$\sqrt{\text{m}}$.

As expected, the rate of crack growth increases monotonically with applied stress-intensity factor. For applied stress-intensity factors below 13.7 MPa$\sqrt{\text{m}}$ no crack propagation was computed after 10^6 seconds. This threshold behavior is consistent with experimental observation [56–59]. At applied stress-intensity factors larger than 41.2 MPa$\sqrt{\text{m}}$, the crack exhibits runaway growth and no equilibrium crack length is found by dynamic relaxation, as expected for applied stress-intensity factors approaching the toughness of the material, $K_{Ic} = 58.4$ MPa$\sqrt{\text{m}}$. Figure 9 shows, over different time scales appropriate to each loading, the computed crack length for applied stress-intensity factors of $K_I = 13.7$, 17.2 and 37.8 MPa$\sqrt{\text{m}}$. Interestingly, each of these cases exhibits distinguishing features of its own. Thus, for the lowest load $K_I = 13.7$ MPa$\sqrt{\text{m}}$, Figure 9a, crack growth is ostensibly continuous and crack-growth initiation is poorly defined and nearly indistinguishable from crack propagation. For the intermediate loading level of 17.2 MPa$\sqrt{\text{m}}$, Figure 9b, crack growth is also ostensibly continuous but the point of crack-growth initiation is clearly discernible as a discontinuity in crack speed. At higher loading levels, such as $K_I = 37.8$ MPa$\sqrt{\text{m}}$, Figure 9c, the crack growth curve has comparatively more structure. Thus, with increasing load crack growth becomes increasingly more intermittent, with quiescent intervals of ostensibly continuous growth punctuated by discrete jumps. This intermittent crack growth is consistent with experimental observation [23] and with the two-dimensional calculations of Serebrinsky et al. [1]. The largest crack jump takes place at initiation, after a certain incubation time, and the amplitude of subsequent jumps decreases monotonically. Crack-growth initiation occurs at a crack advance $\Delta a \approx 200$ μm, or roughly twice the average grain size.

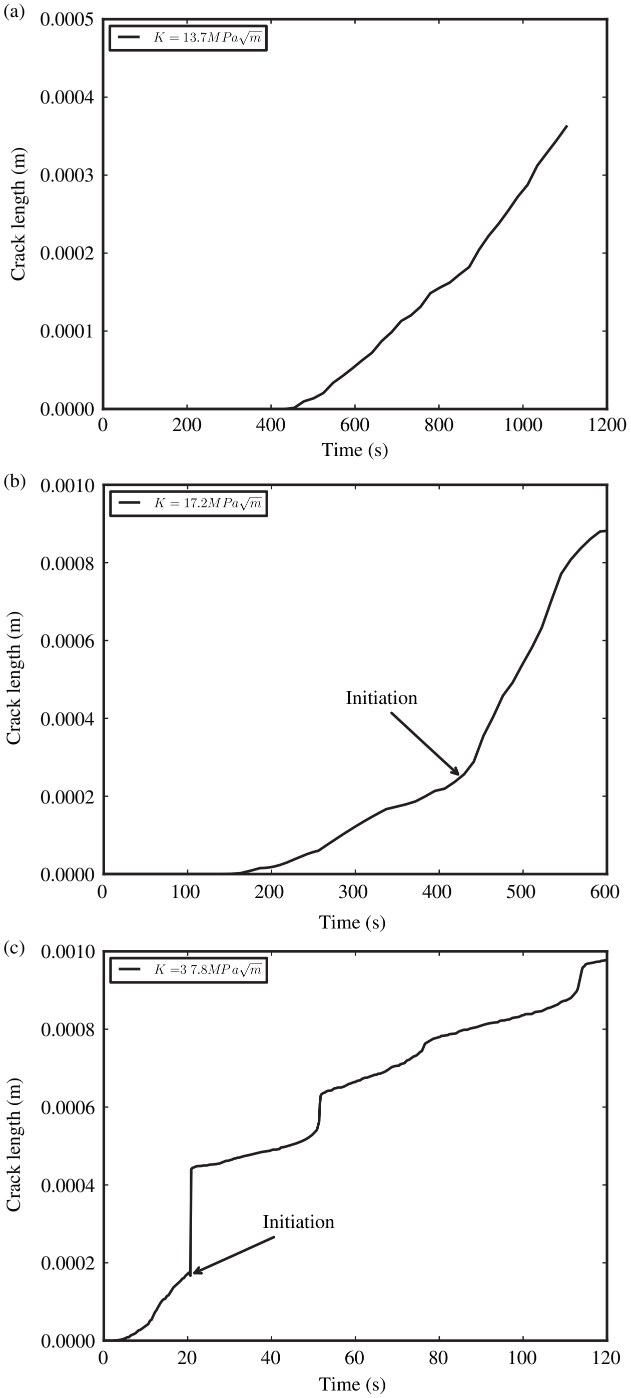

Figure 9. Double-cantilever AISI 4340 steel specimen subjected to a constant applied stress-intensity factor in an aggressive environment. Detail of crack length evolution for applied stress-intensity factors: (a) 13.7 MPa$\sqrt{\text{m}}$; (b) 17.2 MPa$\sqrt{\text{m}}$; and (c) 37.8 MPa$\sqrt{\text{m}}$.

3.4. *Fracture initiation*

For sufficiently high loading, crack growth initiation is evident as a discontinuity in either crack growth rate or crack length, respectively, Figures 9b and c. Figure 10 compares the computed initiation times over a range of applied stress-intensity factors with the experimental values reported in [22]. The comparison is not entirely direct since the experiments were performed on notched specimens, whereas the present model considers a sharp crack. This disparity notwithstanding, the predicted crack initiation times are in fair agreement with experiment. In particular, the model predicts a power-law dependence of the initiation time on the applied stress-intensity factor, in keeping with observation. However, the model tends to over-predict the characteristic exponent of that power-law dependence.

The effect of the grain-boundary diffusion coefficient on the initiation time is illustrated in Figure 11, which compares initiation times for two values of the grain-boundary diffusion coefficient, $D_{gb} = 2.53 \times 10^{-9}$ m^2/sec and $D_{gb} = 1.00 \times 10^{-9}$ m^2/sec. As expected, a reduction in the grain-boundary diffusion coefficient results in longer initiation times, which confirms that diffusion is a rate-limiting mechanism of the model. Interestingly, the reduction in the grain-boundary diffusivity also decreases the characteristic exponent in the power-law dependence of the initiation time on the applied stress-intensity factor, which suggests that the over-prediction of that exponent alluded to above may be due to an over-estimation of the grain-boundary diffusivity. Furthermore, these trends suggest that the grain-boundary diffusivity can be calibrated from initiation time data, but this approach will not be pursued here.

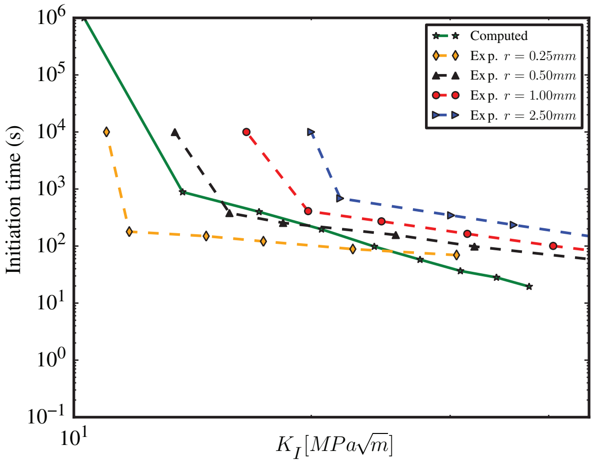

Figure 10. (Color online). Double-cantilever AISI 4340 steel specimen subjected to a constant applied stress-intensity factor in an aggressive environment. Comparison of computed initiation times and experimental data of Hirose and Mura [22] over a range of applied stress-intensity factors. The experimental curves correspond to notch-root radii of 2.5 mm, 1.0 mm, 0.5 mm and 0.25 mm.

3.5. *Crack growth rate*

We conclude by comparing the predicted average crack-growth rates to the experimental data of [23], Figure 12. As may be seen from the figure, the experimental crack-growth rate data for two different heat treatments, resulting in yield stresses $\sigma_y = 1{,}330$ and 1,530 MPa, bound the predicted crack-growth rates

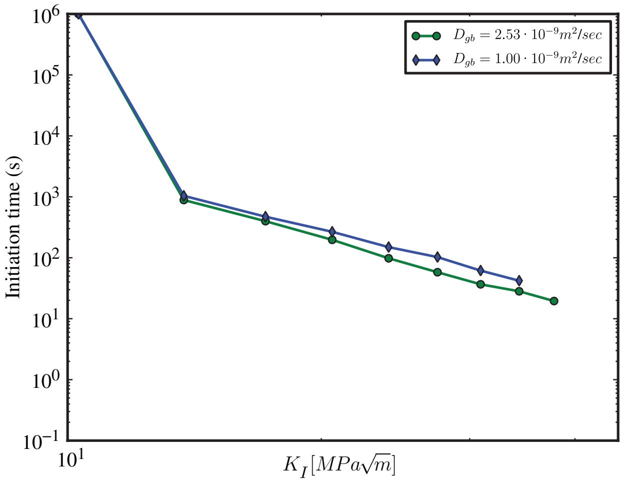

Figure 11. (Color online). Double-cantilever AISI 4340 steel specimen subjected to a constant applied stress-intensity factor in an aggressive environment. Effect of grain boundary diffusion coefficient on initiation time.

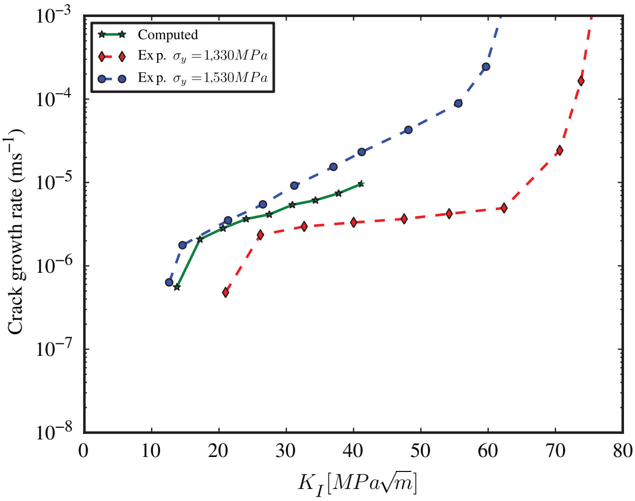

Figure 12. (Color online). Double-cantilever AISI 4340 steel specimen subjected to a constant applied stress-intensity factor in an aggressive environment. Comparison of computed initiation crack-growth curves (green circles) and experimental data of Hirose and Mura [23] over a range of applied stress-intensity factors.

over a broad range of applied stress-intensity factors. In addition to this quantitative agreement, the model correctly predicts a number of salient qualitative features of measured crack-growth rate curves, including: the existence of a threshold intensity factor K_{Iscc} below which there is no crack propagation; a subsequent steeply rising part of the curve known as *stage I*; a plateau, or *stage II*, characterized by a load-insensitive crack-growth rate; and a limiting stress-intensity factor K_{Ic}, or *toughness*, at which pure mechanical failure occurs.

The effect of the grain-boundary diffusion coefficient on crack-growth rates is illustrated in Figure 13, which compares crack-growth rates for two values of the grain-boundary diffusion coefficient, $D_{gb} = 2.53 \times 10^{-9}\,\mathrm{m}^2/\mathrm{sec}$ and $D_{gb} = 1.00 \times 10^{-9}\,\mathrm{m}^2/\mathrm{sec}$. Similarly to the case of crack-growth initiation times, a decrease in grain-boundary diffusivity has the effect of slowing down crack growth, as expected.

4. Summary and concluding remarks

We have formulated a multiscale model for the simulation of hydrogen embrittlement (HE) in metals that accounts for: (i) the degradation of grain-boundary strength that arises from hydrogen coverage; (ii) grain-boundary diffusion of hydrogen; and (iii) a continuum model of plastic deformation that explicitly resolves the three-dimensional polycrystalline structure of the material. The present model extends earlier work by Serebrinsky et al. [1] in several respects, including the three-dimensionality of the model, the addition of grain-boundary diffusion and the explicit resolution of the polycrystalline structure of the material. The increased three-dimensional fidelity of the present model enables a detailed assessment of

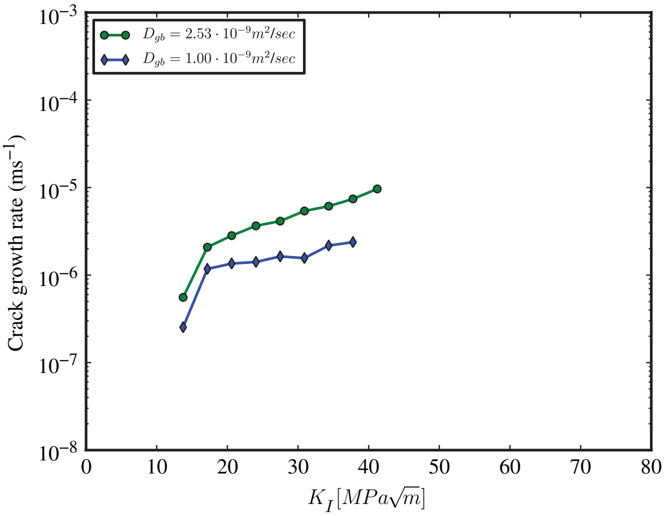

Figure 13. (Color online). Double-cantilever AISI 4340 steel specimen subjected to a constant applied stress-intensity factor in an aggressive environment. Effect of diffusion coefficient on crack growth rate.

the intricate interplay between growing cracks and material microstructure. In particular, calculations suggest that the evolution of the crack surface and the crack front, which is assumed to be intergranular in the present model, is strongly three-dimensional and exhibits phases of crack kinking and trapping, as the crack propagates over and around the grains. The complex interactions between the crack front and individual grains also causes the crack growth to be jerky and unsteady, especially at high applied loads. The full three-dimensionality of the present model also permits consideration of grain anisotropy and texture and plastic deformation of the grains by crystallographic slip. Despite the small size of the computed plastic zone, as expected from the low load levels at which HAC takes place, crystal plasticity does effectively relax the level of stress in the vicinity of the crack tip and partially shields the decohering grain boundaries, thus retarding crack growth. In addition, the explicit resolution of the polycrystalline structure opens the way for the consideration of physical phenomena, such as grain-boundary diffusion, which are difficult to take into account in a two-dimensional model.

Our validation comparisons for AISI 4340 steel suggest that the model is capable of providing qualitative and quantitative predictions that are in general overall agreement with experiment. Overall, the agreement between the model and experimental data is compelling enough to suggest that hydrogen-induced decohesion may be the dominant mechanism of hydrogen-assisted fracture for high strength steels in aqueous environments. In particular, the model enables the calculation of fracture curves characteristic of environment-assisted cracking, such as the crack growth rate as a function of the applied stress-intensity factor. The calculated curves exhibit a number of features, such as thresholds and plateaus, which closely match experimental trends. Such curves in turn provide useful tools for engineering analysis, including life-time prediction of structures and components. To this end, the model can be made material-specific and calibrated in a number of ways. For instance, grain-size distributions and texture can be matched to microscopy measurements; the elastic and plastic properties of the material can be matched to static mechanical tests; and effective or average diffusivities can also be matched to experimental measurements, e.g. initiation-time exponents and stage II crack-growth rates, as demonstrated in Section 3.

An alternative – and perhaps more appealing – route to material specificity is to inform the model using atomistic models and first-principles calculations. Indeed, the present model offers a number of ‘hooks’ for making such connections. For instance, the dependence of grain-boundary cohesion on impurity coverage can be ascertained from first-principles for a variety of host-impurity systems. In addition, the grain-boundary diffusion aspects of the model can be vastly improved by means of first-principles calculations of anisotropic diffusivity constants and their dependence on the individual grain-boundary geometry. The interaction between the host material and the aggressive environment, the dependence of grain-boundary diffusion on grain-boundary separation, and a number of fundamental properties of single-crystal plasticity are also amenable to determination from first-principles in a material-specific way. Each of these enhancements of the model provides fertile grounds and suggests directions for extensive further research.

Acknowledgements

The authors gratefully acknowledge the support of the United States Army Research Office through the award: W911NF-06-0421 Mod/Amend#: P0001.

References

[1] S. Serebrinsky, E.A. Carter and M. Ortiz, J. Mech. Phys. Solids 52 (2004) p.2403.
[2] R.P. Gangloff and M.B. Ives (eds.), *First International Conference on Environment-Induced Cracking of Metals, NACE-10*, Houston, TX, 1990.
[3] A. Turnbull, Corros. Sci. 34 (1993) p.921.
[4] R.H. Jones (eds.), *Chemistry and Electrochemistry of Corrosion and Stress Corrosion Cracking: A Symposium Honoring the Contributions of R.W. Staehle*, Warrendale, PA, 2001.
[5] P. Sofronis, Eng. Fract. Mech. 68 (2001) p.617.
[6] G.E. Kerns, M.T. Wang and R.W. Staehle, *Stress corrosion cracking and hydrogen embrittlement in high strength steels*, in *Stress Corrosion Cracking and Hydrogen Embrittlement of Iron Based Alloys, NACE-5*, R.W. Staehle, J. Hochmann, R.D. McCright and J.E. Slater, eds., Houston, TX, 1977, p.700.
[7] P.G. Marsh and W.W. Gerberich, *Stress corrosion cracking of high-strength steels*, in *Stress-Corrosion Cracking*, R.H. Jones, ed., ASM International, Materials Park, OH, 1992, p.63.
[8] J. Völkl and G. Alefeld (eds.), *Hydrogen in Metals – Basic Properties*, *Topics in Applied Physics*, Vol. 28, Springer-Verlag, Berlin, 1978.
[9] Y. Fukai, *The Metal–Hydrogen System: Basic Bulk Properties*, Springer-Verlag, Berlin, 1993.
[10] P. Sofronis and R.M. McMeeking, J. Mech. Phys. Solids 37 (1989) p.317.
[11] A. Turnbull, D.H. Ferriss and H. Anzai, Mat. Sci. Eng. A 206 (1996) p.1.
[12] A. Turnbull, Corrosion 57 (2001) p.175.
[13] H.K. Birnbaum, *Mechanisms of hydrogen-related fracture of metals*, in *First International Conference on Environment-Induced Cracking of Metals, NACE-10*, R.P. Gangloff and M.B. Ives, eds., Houston, TX, 1990, p. 21.
[14] D.G. Westlake, Trans. ASM 62 (1969) p.1000.
[15] H.G. Nelson, Metall. Trans. A 7A (1976) p.621.
[16] R.A. Oriani, *Hydrogen effects in high-strength steels*, in *First International Conference on Environment-Induced Cracking of Metals, NACE-10*, R.P. Gangloff and M.B. Ives, eds., Houston, TX, 1990, p.439.
[17] C.D. Beachem, Metall. Trans. 3 (1972) p.437.
[18] H.K. Birnbaum and P. Sofronis, Mat. Sci. Eng. A 176A (1994) p.191.
[19] A.R. Troiano, Trans. ASM 52 (1960) p.54.
[20] R.A. Oriani, Berichte der Bunsengesellschraft für Physikalische Chemie 76 (1972) p.848.
[21] R.A. Oriani and P.H. Josephic, Acta Metall. 25 (1977) p.979.
[22] Y. Hirose and T. Mura, Eng. Fract. Mech. 19 (1984) p.317.
[23] Y. Hirose and T. Mura, Eng. Fract. Mech. 19 (1984) p.1057.
[24] D.E. Jiang and E.A. Carter, Acta Mater. 52 (2004) p.4801.
[25] A. Hatcher, *Algebraic Topology*, Cambridge University Press, Cambridge, 2002.
[26] K. Barmak, D. Kinderlehrer, I. Livshits and S. Ta'asan, *Remarks on a multiscale approach to grain growth in polycrystals*, in *Progress in Nonlinear Differential Equations and Their Applications Variational Problems in Materials Science*, G. dal Maso, A. de Simone and F. Omarelli, eds., Birkäuser, Basel, 2006, p.1.

[27] K. Barmak, M. Emelianenko, D. Golovaty, D. Kinderlehrer and S. Ta'asan, SIAM J. Sci. Comput. 30 (2008) p.3150.

[28] M. Groeber, A. Ghoshb, M.D. Uchicc and D.M. Dimiduk, Acta Mater. 56 (2008) p.1257.

[29] G.S. Rohrr, J. Gruber and A.D. Rollett, *Distributions in polycrystalline materials*, in *Materials Processing and Texture*, A.D. Rollett, ed., John Wiley, Hoboken, NJ, 2009, p.343.

[30] *Military Handbook 5H: Metallic Materials and Elements for Aerospace Vehicle Structures*, US Department of Defense, 1998.

[31] M. Ortiz and E.P. Popov, Internat. J. Numer. Meth. Eng. 21 (1985) p.1561.

[32] M. Ortiz and L. Stainier, Comput. Meth. Appl. Mech. Eng. 171 (1999) p.419.

[33] J.C. Fisher, J. Appl. Phys. 22 (1951) p.74.

[34] Y. Mishin and C. Herzig, Mater. Sci. Eng. A 260 (1999) p.55.

[35] A. Atkinson, J. Chem. Soc. Faraday Trans. 86 (1990) p.1307.

[36] L.G. Harrison, Trans. Faraday Soc. 57 (1961) p.1191.

[37] A.C.T. Van Duin and W.A. Goddard III, Private communication: Unpublished calculations carried out under Army Research Office award W911NF-06-0421 (2008).

[38] A.C.T. Van Duin and S.R. Larter, Organ. Geochem. 29 (1998) p.043.

[39] A.C.T. Van Duin, B.V. Merinov, S.S. Han and W.A. Goddard III, J. Phys. Chem. A 112 (2008) p.3133.

[40] A.C.T. Van Duin, B.V. Merinov, S.S. Han, C.O. Dorso and W.A. Goddard III, J. Phys. Chem. A 112 (2008) p.11414.

[41] R.W. Balluffi, S.M. Allen and W.C. Carter, *Kinetics of Materials*, Wiley-Interscience, Hoboken, NJ, 2005.

[42] J.R. Galvele, Corros. Sci. 21 (1981) p.551.

[43] S.M. Sharland and P.W. Tasker, Corros. Sci. 28 (1988) p.603.

[44] O.T. Nguyen, *Cohesive models of fatigue crack growth and stress-corrosion cracking*, *PhD thesis*, California Institute of Technology, Pasadena, CA, 2000.

[45] M. Lu, P.S. Pao, T.W. Weir, G.W. Simmons and R.P. Wei, Metall. Trans. A 12A (1981) p.805.

[46] J.H. Rose, J.R. Smith, F. Guinea and J. Ferrante, Phys. Rev. B 29 (1984) p.2963.

[47] A. van der Ven and G. Ceder, Phys. Rev. B 67 (2003) p.060101-1-4.

[48] M. Ortiz and A. Pandolfi, Internat. J. Numer. Meth. Eng. 44 (1999) p.1267.

[49] G.T. Camacho and M. Ortiz, Internat. J. Solids Struct. 33 (1996) p.2899.

[50] O. Nguyen and M. Ortiz, J. Mech. Phys. Solids 50 (2002) p.1727.

[51] C.D. Beachem, Metall. Mater. Trans. B 3 (1972) p.441.

[52] D. Chapelle and K.J. Bathe, Comput. Struct. 47 (1993) p.537.

[53] C.A. Felippa, K.C. Park and C. Farhat, Comput. Meth. Appl. Mech. Eng. 190 (2001) p.3247.

[54] P. Underwood, *Dynamic relaxation*, in *Computational Methods for Transient Analysis*, T. Belytschko and T.J.R. Hughes, eds., Elsevier Science, New York, 1983, p.246.

[55] D.R. Oakley and N.F. Knight, Comput. Meth. Appl. Mech. Eng. 126 (1995) p.67.

[56] Y. Hirose and T. Mura, Eng. Fract. Mech. 19 (1984) p.1057.

[57] G.W. Simmons, P.S. Pao and R.P. Wei, Met. Trans. A 9A (1978) p.1147.

[58] V.J. Colangelo and M.S. Ferguson, Corrosion 25, 12 (1969) p.509.

[59] W.B. Lisagor, *Influence of precracked specimen configuration and starting stress intensity on the stress corrosion cracking of 4340 steel*, in *Environment-Sensitive Fracture – Evaluation and Comparison of Test Methods*, S.W. Dean, E.N. Pugh and G.M. Ugiansky, eds., ASTM–STP 821, ASTM Philadelphia, PA, 1984, p.80.